

## CHEMISTRY

# Patterning the consecutive Pd<sub>3</sub> to Pd<sub>1</sub> on Pd<sub>2</sub>Ga surface via temperature-promoted reactive metal-support interaction

Yiming Niu<sup>1,2†</sup>, Yongzhao Wang<sup>1,2†</sup>, Junnan Chen<sup>1,2</sup>, Shiyan Li<sup>3</sup>, Xing Huang<sup>4,5</sup>, Marc-Georg Willinger<sup>4,6</sup>, Wei Zhang<sup>7\*</sup>, Yuefeng Liu<sup>3\*</sup>, Bingsen Zhang<sup>1,2,3\*</sup>

Atom-by-atom control of a catalyst surface is a central yet challenging topic in heterogeneous catalysis, which enables precisely confined adsorption and oriented approach of reactant molecules. Here, exposed surfaces with either consecutive Pd trimers (Pd<sub>3</sub>) or isolated Pd atoms (Pd<sub>1</sub>) are architected for Pd<sub>2</sub>Ga intermetallic nanoparticles (NPs) using reactive metal-support interaction (RMSI). At elevated temperatures under hydrogen, in situ atomic-scale transmission electron microscopy directly visualizes the refaceting of Pd<sub>2</sub>Ga NPs from energetically favorable (013)/(020) facets to (011)/(002). Infrared spectroscopy and acetylene hydrogenation reaction complementarily confirm the evolution from consecutive Pd<sub>3</sub> to Pd<sub>1</sub> sites of Pd<sub>2</sub>Ga catalysts with the concurrent fingerprinting CO adsorption and featured reactivities. Through theoretical calculations and modeling, we reveal that the restructured Pd<sub>2</sub>Ga surface results from the preferential arrangement of additionally reduced Ga atoms on the surface. Our work provides previously unidentified mechanistic insight into temperature-promoted RMSI and possible solutions to control and rearrange the surface atoms of supported intermetallic catalyst.

## INTRODUCTION

Active site geometry enables a delicate manipulation of the adsorption, migration, and reaction of reactants in heterogeneous catalysis. Thus, the exceptional catalytic performance can be obtained via controlling of the active metals with specific geometries. The general solutions adopt the strong binding between metal and support, the alloy diluting of active metal in inert metal matrixes, or the metal precursor with specific coordination configurations, to control the surface atoms as the desired geometries, such as atomic-ensemble [Fe<sub>2</sub>/mpg-C<sub>3</sub>N<sub>4</sub> (1), Pt<sub>1</sub>-Pt<sub>n</sub>/α-MoC (2), and Pt<sub>3</sub>/Co@Pd (3)], single-atom [Pt<sub>1</sub>/FeO<sub>x</sub> (4), Pt<sub>1</sub>/CeO<sub>2</sub> (5), and Pt<sub>1</sub>/α-MoC (6)], single-atom alloy [Pd<sub>1</sub>Cu (7), Pd<sub>1</sub>Au (8), and Pd<sub>1</sub>Ni (9)], and hetero-atomic pair [Ni/Fe-N-C (10) and Ir<sub>1</sub>Mo<sub>1</sub>/TiO<sub>2</sub> (11)]. These ensemble or isolated metal sites are powerful to yield some subtle catalytic behavior control in various heterogeneous reactions, ranging from selective hydrogenation reactions (7, 11, 12), water-gas shift reaction (2), CO oxidation (4), three-way catalytic reactions (13), alkene epoxidation reaction (1), to electrocatalytic oxygen reduction reaction (3). However, it remains challenging for controlling the specific active metal as desired geometries with

high homogeneity without applying multiple synthetic procedures or complex precursors.

In principle, intermetallic compounds can afford various active metal geometries depending on some specific surface, attributed to their highly ordered structures compared to pure metals or solid solution alloys. A typical example is the PdGa (111) and (111) planes, which hold individual Pd trimers and isolated Pd-atom geometries in one single crystal surface (14). Intermetallic nanocrystals were also prepared with specific morphologies, such as cubic, octahedral, or tetrahedral of Pt<sub>3</sub>Ni and PtPd to expose certain surfaces in catalysis (15, 16). However, these well-shaped nanocrystals generally require surfactants to stabilize the desired facets during the growth. It leads to the difficulty to remove these surfactants, which bind with surface sites and obscure the active metal geometries, with no changes of the surface. Among various methods of preparing intermetallic compounds, a reactive metal-support interaction (RMSI) has been demonstrated as an effective approach. It is of great interests to in situ faceting the nanoparticles (NPs) with desired surfaces and active metal geometries via controlling the interaction between the intermetallic nanocrystals and oxide supports. However, it is challenging, as it highly depends on the mechanistic understanding of formation and evolution of the supported intermetallic under chemical environments.

Generally, the surface structure of catalysts depends on their chemical environment and can thus differ between reactive state and conditions applied during ex situ characterizations. This can lead to an ambiguous recognition of the active structure and set limits to an establishment of reliable structure-performance relationship in catalysis. It is essential to study the actual in situ structural formation and evolution of catalyst under working conditions. Recently, in situ transmission electron microscopy (TEM) with spectroscopy accessories has emerged as an effective solution to identify the catalyst structure and its possible evolution under working conditions (17–19). It enables further reducing the

<sup>1</sup>Shenyang National Laboratory for Materials Science, Institute of Metal Research, Chinese Academy of Sciences, Shenyang 110016, China. <sup>2</sup>Department of Materials Science and Engineering, University of Science and Technology of China, Shenyang 110016, China. <sup>3</sup>Dalian National Laboratory for Clean Energy, Dalian Institute of Chemical Physics, Chinese Academy of Sciences, Dalian 116023, China. <sup>4</sup>Scientific Center for Optical and Electron Microscopy, ETH Zurich, Otto-Stern-Weg 3, Zurich 8093, Switzerland. <sup>5</sup>College of Chemistry, Fuzhou University, Fuzhou 36108, China. <sup>6</sup>School of Natural Science (NAT), Department of Chemistry, Technical University of Munich, Lichtenbergstraße 4, Garching 85747, Germany. <sup>7</sup>School of Materials Science and Engineering, Key Laboratory of Automobile Materials MOE, and Electron Microscopy Center, Jilin Provincial International Cooperation Key Laboratory of High-Efficiency Clean Energy Materials, Jilin University, Changchun 130012, China.

\*Corresponding author. Email: weizhang@jlu.edu.cn (W.Z.); yuefeng.liu@dicp.ac.cn (Y.L.); bszhang@imr.ac.cn (B.Z.)

†These authors contributed equally to this work.

materials/pressure gap, especially superior in surface and interface structural identification of those industrial catalysts. In situ TEM has allowed direct visualization of some typical phenomena related to the active structure formation and evolution under relevant conditions, such as formation of strong (S)MSI state in Pt-TiO<sub>2</sub> system (20, 21), oscillatory behavior of Pt during catalysis (22), gas molecules adsorption on catalyst surface (23, 24), refaceting of NPs (25–27), and interfacial intermediated formation of intermetallic (28). The development of catalysis and materials enables being largely promoted.

Here, we report an arrangement of surface atoms through applying temperature-promoted RMSI to the supported Pd<sub>2</sub>Ga NPs, assisted by in situ TEM and spectroscopies. In situ annular dark-field scanning (ADF-S) TEM with atomic-scale energy-dispersive x-ray (EDX) elemental mapping directly identifies the highly ordered orthorhombic structure of Pd<sub>2</sub>Ga NPs subjected to the RMSI. Pd<sub>2</sub>Ga NPs are then found with an evolution from (013)/(020) to (011)/(002) facets at higher temperatures, reflecting the continuous arrangements of Pd trimers (Pd<sub>3</sub>) to isolated Pd (Pd<sub>1</sub>) on the surface. In situ CO adsorption diffuse reflectance infrared Fourier transformed spectroscopy (CO-DRIFTS) results provide complementary evidence regarding the transition from bridge to on-top adsorption sites. Moreover, the surface energies of different facets are calculated to construct the Wulff shape of Pd<sub>2</sub>Ga NP. The proportion of gallium in the atomic model of Pd<sub>2</sub>Ga NPs encapsulated with gallium-rich facets exceeds the stoichiometric ratio. Thus, the additional Ga atoms reduced from support at higher temperatures is mainly responsible for restructuring of the Pd<sub>2</sub>Ga surface. In addition, acetylene hydrogenation is adopted as a model reaction during which Pd<sub>3</sub> and Pd<sub>1</sub> sites exhibit respective high activity or high surface atomic efficiency. The surface atom arrangements in Pd/Ga<sub>2</sub>O<sub>3</sub> catalyst not only provide a mechanistic insight into the interaction between the metal and support but also demonstrate an effective and facile approach to delicately tune the surface structure of intermetallic catalysts.

## RESULTS

### In situ observation of the RMSI-induced formation of Pd<sub>2</sub>Ga

Attributed to the RMSI, Pd<sub>2</sub>Ga can be generated from the reduction of gallium oxide and supported Pd (29). Thus, oxide nanorods were chosen for homogeneous anchoring of Pd, which also facilitates recording of in situ TEM experiments. Initially, GaOOH nanorods were prepared via a solvothermal method (see the experimental details in Materials and Methods) (29, 30). By using TEM and x-ray diffraction (XRD), the morphology and structure were demonstrated (fig. S1). GaOOH transformed to  $\alpha$ -Ga<sub>2</sub>O<sub>3</sub>, mixed  $\alpha$ -Ga<sub>2</sub>O<sub>3</sub>/ $\beta$ -Ga<sub>2</sub>O<sub>3</sub>, and  $\beta$ -Ga<sub>2</sub>O<sub>3</sub> after 500°, 700°, and 900°C calcination, respectively (fig. S2). The pure  $\alpha$ -Ga<sub>2</sub>O<sub>3</sub> was selected as the support to obtain the desired Pd<sub>2</sub>Ga phase (29, 31). After impregnation and calcination at 500°C, the Ga<sub>2</sub>O<sub>3</sub> maintains the rod-like morphology with nanopores and PdO NPs are uniformly distributed on the support (fig. S3). Then, the PdO/Ga<sub>2</sub>O<sub>3</sub> was subjected to elevated temperatures from 100° to 600°C under H<sub>2</sub>/He atmosphere. As a result, PdO was reduced to Pd, Pd<sub>2</sub>Ga, and Pd<sub>2</sub>Ga/Pd<sub>5</sub>Ga<sub>3</sub> at 100° to 200°, 300° to 500°, and 600°C, respectively. The cubic Pd and orthorhombic Pd<sub>2</sub>Ga (Fig. 1A) are identified from their featured (200) and (020), (203) diffraction peaks located at 46.7° and 44.2°, 47.4° in XRD patterns (Fig. 1B), respectively. Ex situ high-resolution

transmission electron microscope (HRTEM) with simulated selected area electron diffraction (SAED) image also confirms the formation of Pd<sub>2</sub>Ga phase with an overlayer of GaO<sub>x</sub> due to the surface oxidation upon exposure to air (fig. S4) (32, 33). At higher reduction temperatures, more gallium atoms are reduced from the Ga<sub>2</sub>O<sub>3</sub> support and diffuse into the NPs, which results in the formation of Pd<sub>5</sub>Ga<sub>3</sub> (fig. S5). Meanwhile, the monoclinic  $\alpha$ -Ga<sub>2</sub>O<sub>3</sub> remains until 500°C (Fig. 1B) and partially transformed to hexagonal  $\beta$ -Ga<sub>2</sub>O<sub>3</sub> after 600°C reduction (fig. S5A), which is well consistent with the TEM analysis (fig. S6). HRTEM combining SAED simulation results confirm the coexistence of Pd<sub>2</sub>Ga and Pd<sub>5</sub>Ga<sub>3</sub> NPs after 600°C reduction (figs. S7 and S8), which are also encapsulated with oxide layers after contacting with air during ex situ experiments. Therefore, in situ TEM experiments enable accurately elucidating the structural evolution of Pd/Ga<sub>2</sub>O<sub>3</sub> during RMSI. As shown in figs. S9 and S10, Pd<sub>2</sub>Ga forms in the left of the Pd NPs and grows gradually proceeding into the interior. That is, the Pd<sub>2</sub>Ga structure grows along the direction of Pd <200>, ultimately transforming completely into the Pd<sub>2</sub>Ga structure at elevated temperatures. Such phase transformation is supposed to be concurrently induced by both the reduction of Ga<sub>2</sub>O<sub>3</sub> at the interface and thereof the subsequent diffusion of Ga atoms. It is quite similar to the formation of PdZn in the Pd-ZnO catalyst (28). The morphology and crystal structure of Ga<sub>2</sub>O<sub>3</sub> support are well maintained (figs. S11 and S12). The in situ reduced Pd NPs exhibit an average particle size of 4.9 ± 1.4 nm, which are homogeneously and preferentially distributed on the pores of Ga<sub>2</sub>O<sub>3</sub> (Fig. 1C and figs. S13 to S15). Through the further reduction of Ga<sub>2</sub>O<sub>3</sub> and formation of Pd<sub>2</sub>Ga intermetallic at 500°C, it increased slightly (5.8 ± 1.5 nm; Fig. 1D).

### Atomic-scale structural characterization of Pd<sub>2</sub>Ga

As mentioned above, the Pd-Ga<sub>2</sub>O<sub>3</sub>-based structures were identified after reduction at the temperature range of 100° to 600°C. The microstructural evolution during the phase transition process in RMSI was monitored by in situ TEM. Initially, PdO was reduced to Pd under 300 Pa H<sub>2</sub> at 200°C and exhibited as cuboctahedrons, which were exposed with (111), (200), and (110) facets (Fig. 2A and fig. S16). Partial Pd NPs maintained their face-centered cubic structure even with a further increased temperature to 300°C (fig. S17) during in situ experiments, which was ascribed to the low pressure in environmental TEM (ETEM). Therefore, ex situ experiment was conducted at 300°C under 100 Pa H<sub>2</sub> to confirm the delayed formation of Pd<sub>2</sub>Ga (fig. S18). As it increased to 400°C in ETEM, the transformation of Pd to Pd<sub>2</sub>Ga was observed with a slightly increased particle size. The formed Pd<sub>2</sub>Ga NP was mainly enclosed with (013), (202), (211), and (215) facets (Fig. 2D). The corresponding fast Fourier transforms (FFTs) demonstrate the single crystalline nature of Pd and Pd<sub>2</sub>Ga NPs viewed from [01 $\bar{1}$ ] and [1 $\bar{3}$ 1] directions, respectively. The atomic models in Fig. 2 (C and F) display the morphological evolution of the identical NP. Subsequently, in situ ADF-STEM was conducted to identify the highly ordered orthorhombic Pd<sub>2</sub>Ga structure due to its sensitivity to Z contrast (Z = 46 and 31 for Pd and Ga, respectively) (32). As the pressure of H<sub>2</sub> lowered to 10 Pa during in situ STEM studies, the formation of Pd<sub>2</sub>Ga structure was further delayed to 500°C. The formed Pd<sub>2</sub>Ga NPs were carefully analyzed through the measured d-spacings and angles between lattice planes in ADF-STEM images (fig. S19). Thus,

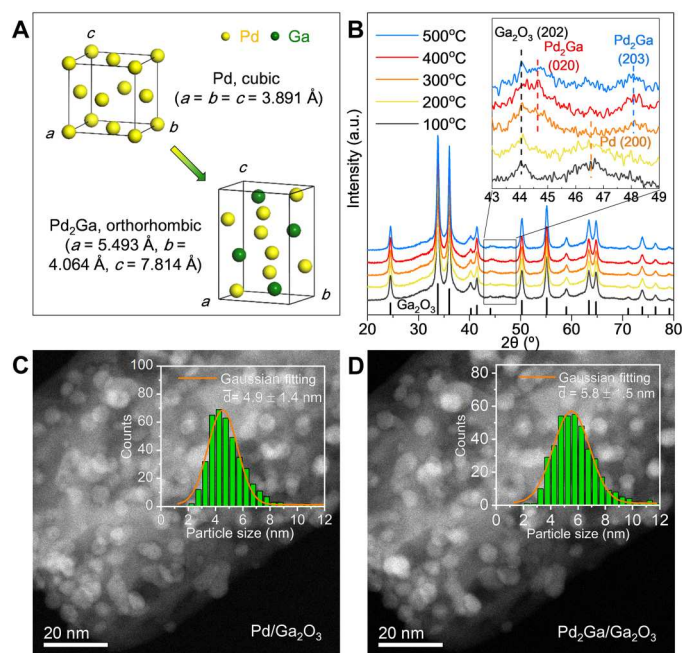


**Fig. 1.** RMSI promoted Pd<sub>2</sub>Ga intermetallic. (A) Unit cells of Pd and Pd<sub>2</sub>Ga. a.u., arbitrary units. (B) Powder XRD patterns of 5.0 weight % (wt %) Pd/Ga<sub>2</sub>O<sub>3</sub> samples after reduction at different temperatures (100° to 500°C from bottom to top) under H<sub>2</sub> atmosphere, respectively. The black lines are indexed as α-Ga<sub>2</sub>O<sub>3</sub> (JCPDS, 43-1013). The inset is the enlarged area from 43° to 49°. (C and D) In situ ADF-STEM images of Pd/Ga<sub>2</sub>O<sub>3</sub> after reduction at 200° and 500°C, respectively. The top-right insets are the corresponding particle size distribution histograms of Pd and Pd<sub>2</sub>Ga NPs, and the orange line is the Gaussian fitting curve.

the Pd<sub>2</sub>Ga NPs captured from  $[1\bar{3}1]$ ,  $[1\bar{4}3]$ ,  $[\bar{1}01]$ , and  $[3\bar{3}\bar{1}]$  zone axes were identified, respectively. These ADF-STEM images were enlarged and displayed (Fig. 2, G, I, and K, and fig. S20) to further identify the highly ordered Pd<sub>2</sub>Ga structure. As shown in Fig. 2G, the bright dots represent the atomic columns viewed from  $[1\bar{3}1]$  zone axis and directly interpreted by the STEM simulation and corresponding atomic model (Fig. 2H), which displays an inhomogeneous contrast distribution that is consistent with the location of Pd and Ga, where the bright and dark parts are mainly composed of Pd and Pd/Ga atoms, respectively. The adjacent atomic columns show a 180° rotational symmetry relationship as marked in Fig. 2 (G and H), thus demonstrating zigzag intensity curves of (013) planes. Viewed from  $[1\bar{4}3]$  zone axis, the alternating light and dark dotted lines were identified as (111) planes, which are composed of either Pd or Pd/Ga atoms (Fig. 2I). Two levels of brightness were observed for atomic columns containing either Pd or Pd/Ga columns, consistent with the STEM simulation and atomic model (Fig. 2J). As shown in Fig. 2K, the featured angle between (202) and (020) planes is composed of alternative arrangement of light and dark spots observed from  $[\bar{1}01]$  zone axis, which also matched well with the atomic model (Fig. 2L) and simulated STEM image (Fig. 2M). The simulated SAED images [bottom-right insets in Fig. 2 (H, J, and L)] are well consistent with the corresponding FFTs in  $[1\bar{3}1]$ ,  $[1\bar{4}3]$ , and  $[\bar{1}01]$  directions, respectively. Moreover, EDX elemental mapping (Fig. 2N) was conducted after the removal of the H<sub>2</sub> atmosphere, demonstrating the elementary composition and distribution of atom-by-atom Pd and Ga. These

results unambiguously prove that the highly ordered orthorhombic Pd<sub>2</sub>Ga was formed under in situ conditions, consistent with our previous ex situ studies (29).

### Refacetting of Pd<sub>2</sub>Ga promoted by RMSI

XRD and in situ TEM have evidenced the formation of highly ordered Pd<sub>2</sub>Ga structure after reduction. Thus, the microstructural evolution of Pd<sub>2</sub>Ga was monitored through ETEM at elevated temperatures. Here, electron dose rate less than 300 e<sup>-</sup>Å<sup>2</sup> s<sup>-1</sup> was adopted during the HRTEM observation to avoid the possible damage from the high-energy electron beam according to our previous studies (34). One identical NP located on the edge of supports was selected to elucidate the ongoing surface variation (fig. S21). As shown in Fig. 3 (A to C), the NP morphology changed from 400° to 500°C. The Pd<sub>2</sub>Ga NPs were generated after 400°C reduction at 300 Pa under H<sub>2</sub> atmosphere. The selected Pd<sub>2</sub>Ga intermetallic NP was also identified by measuring the lattice d-spacing and their acute angles, demonstrating that the NP was mainly exposed with (013) and (020) in Fig. 3A. The corresponding FFT exhibits the single-crystalline nature of the Pd<sub>2</sub>Ga NP viewed from  $[100]$  and well consistent with the simulated SAED. As it increased to 500°C, the Pd<sub>2</sub>Ga NPs started refacetting (Fig. 3B), during which the top area turned to flat and the (013)/(020) facets are partially reduced. The newly appeared facets were identified as Pd<sub>2</sub>Ga (011) according to the measured d-spacing and the angles with (013) and (020) planes. More (013) and (020) facets were continuously transferred to (011) at 500°C, as shown in Fig. 3C. The enlarged HRTEM images acquired from the line box in Fig. 3 (A to C) overlapped with atomic models clearly displaying the facet evolution of Pd<sub>2</sub>Ga (Fig. 3, D to F). Simulated HRTEM results also confirm that the (013)/(020) transform to (011) facets at the top area of the observed Pd<sub>2</sub>Ga NP for higher temperatures (Fig. 3, G to I). Similarly, in the bottom-right area of the NP, the (013) facets gradually change to (002) facets during this process. Therefore, the aforementioned results demonstrate that the (013) and (020) facets of Pd<sub>2</sub>Ga NP transform to (011) and (002) facets from 400° to 500°C during in situ TEM experiments.

### Surface atomic arrangement and evolution of Pd<sub>2</sub>Ga during refacetting

Subsequently, the surface atom arrangement and evolution during this process were analyzed according the crystalline structure of Pd<sub>2</sub>Ga. The (013), (020), (011), and (002) surfaces were cleaved from Pd<sub>2</sub>Ga (orthorhombic,  $a = 5.493$  Å,  $b = 4.064$  Å, and  $c = 7.814$  Å), and the surface atomic arrangements of Pd were clarified. The side view of these surfaces (fig. S22) demonstrates that (013)/(020) and (011)/(002) are close-packed and non-close-packed surfaces, respectively. The arrangement of Pd atoms on (013) and (020) is quite similar, in which three Pd atoms form a triangle and then connect at the apex to form a zigzag shape (Fig. 3, J and K). However, the distances between the Pd atoms are slightly different. The distances between the adjacent Pd atoms on (013) plane are 2.81, 2.82, and 2.90 Å, which slightly increase to 2.81, 2.85, and 2.99 Å on (020) plane. Pd atoms in the linear arrangement exhibits the shortest distance of 2.81 Å, while the distance between Pd atoms is slightly larger on both the sides of the zigzag shape. The arrangement of Pd atoms differs completely from those when Pd<sub>2</sub>Ga refacitted to (011) and (002). The Pd atoms are separated by the surrounding Ga atoms, and the

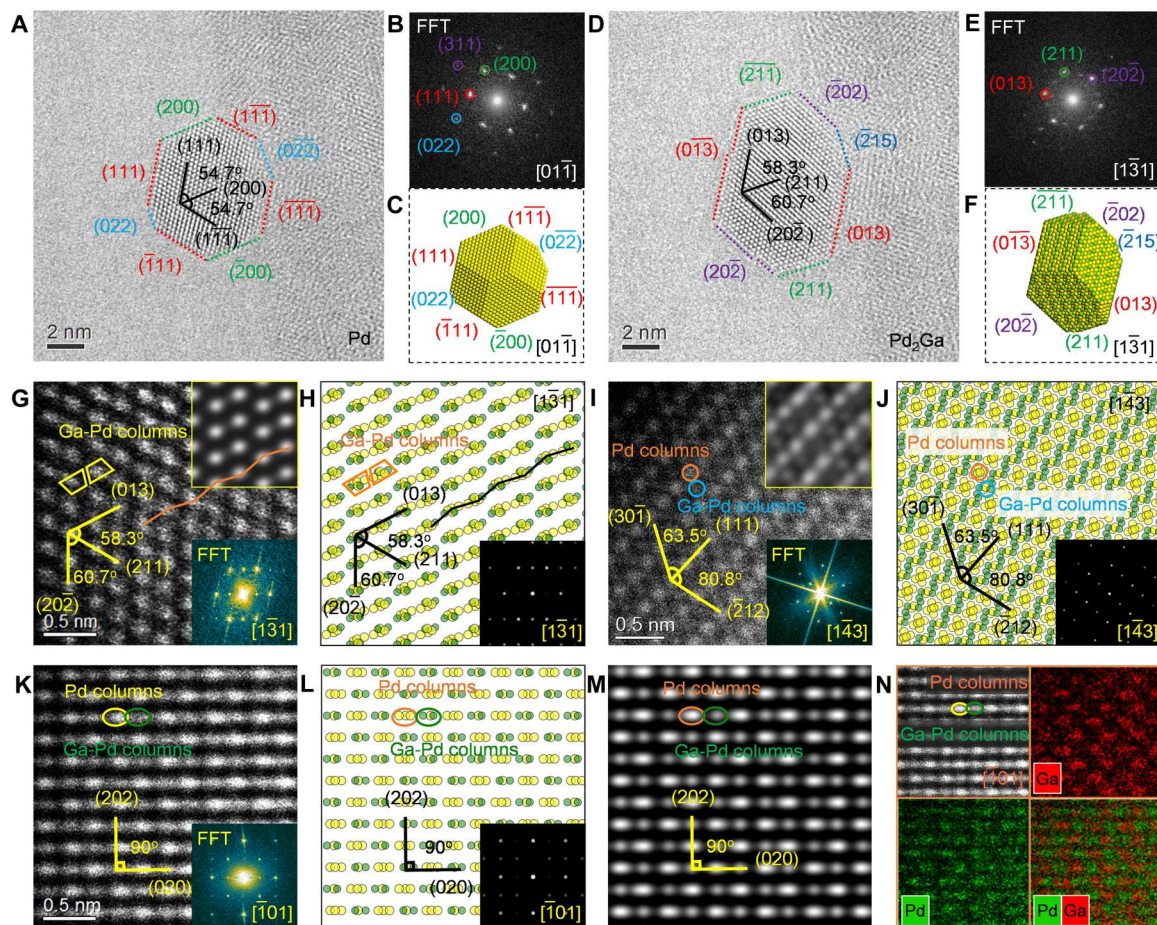


**Fig. 2. Atomic-scale structural identification of Pd<sub>2</sub>Ga.** In situ HRTEM images of identical Pd-based NP at 200°C (A) and 400°C (D). (B) and (C) and (E) and (F) are the corresponding FFTs and atomic models of (A) and (D). In situ ADF-STEM images of Pd<sub>2</sub>Ga observed from [131] (G), [143] (I), and [101] (K) directions with corresponding atomic models (H, J, and L). Yellow and green balls in (H), (J), and (L) represent Pd and Ga atoms, respectively. The top-right insets in (G) and (I) are the corresponding simulated ADF-STEM images. The bottom-right insets in (G), (I), and (K) and (H), (J), and (L) are the corresponding FFT and simulated SAED images, respectively. (M) Simulated ADF-STEM image along the [101] of Pd<sub>2</sub>Ga. (N) ADF-STEM with corresponding atomic-resolution EDX elemental-mapping images of Ga (red) and Pd (green).

nearest Pd atom distances are 4.06, 4.49, and 5.48 Å, respectively (Fig. 3, L and M). As a result, the surface atomic configuration is Pd<sub>1</sub>. Therefore, the results exhibit that the initially generated Pd<sub>2</sub>Ga NPs are mainly composed of continuous Pd<sub>3</sub> atom arrangement on the surface. It transforms to Pd<sub>1</sub> sites at elevated temperatures. More evidences observed from [362] and [001] axes also demonstrated this refaceting phenomenon of Pd<sub>2</sub>Ga structure under elevated temperatures (figs. S23 and S24).

In situ TEM could directly image the surface dynamics at the atomic scale. However, it is still not fully convinced using two-dimensional projection of limited amounts NPs to interpret the variation Pd<sub>2</sub>Ga surface arrangements. Thus, in situ CO adsorption DRIFTS experiments were used to complementarily and generally clarify the surface atom arrangement and variation. There are three kinds of CO adsorption sites on the pure Pd, classified as hollow (1800 to 1900 cm<sup>-1</sup>), bridge (1900 to 2000 cm<sup>-1</sup>), and on-top (2000 to 2100 cm<sup>-1</sup>) sites according to previous studies (35, 36). As shown in Fig. 3N, the Pd/Ga<sub>2</sub>O<sub>3</sub> catalysts exhibit the dominated bridge and hollow adsorbed CO adsorption on Pd, as well as only little linearly adsorbed CO. In addition, the overall peak shifts

toward higher wave numbers as CO coverage increases because of the weakening of Pd-CO interaction by the lateral CO-CO interactions at high coverages (35). The surface atom arrangement of Pd is markedly changed as of the Pd<sub>2</sub>Ga formation, and only the on-top and bridge sites were observed in CO-DRIFTS results (Fig. 3O), in good agreement with the previous study (37). The absence of hollow adsorption of CO was ascribed to the increased distance between Pd atoms on Pd<sub>2</sub>Ga. Distances of 2.8 to 3.0 Å on Pd<sub>2</sub>Ga (013) and (020) facets are identified, which are slightly larger than Pd (111) (2.75 Å). It was speculated that CO is preferentially bridged adsorbed on the adjacent Pd atoms with 2.81 Å distances. Generally speaking, the linearly adsorbed CO generally locates on the Pd atoms, 2.9 to 3.0 Å away from other Pd atoms. The theoretical surface atom arrangement of Pd on Pd<sub>2</sub>Ga (013)/(020) facets is consistent with the experimental CO-DRIFTS results. It exhibits a comparable amount of linearly and bridge-adsorbed CO on Pd<sub>2</sub>Ga generated after reduction at 300°C. As it increases to 500°C, only linearly adsorbed CO was observed on Pd<sub>2</sub>Ga. It implies that the fully isolated Pd<sub>1</sub> atoms exist on the Pd<sub>2</sub>Ga surface (Fig. 3P). The CO-DRIFTS at different partial pressures of CO and after removing the gaseous CO

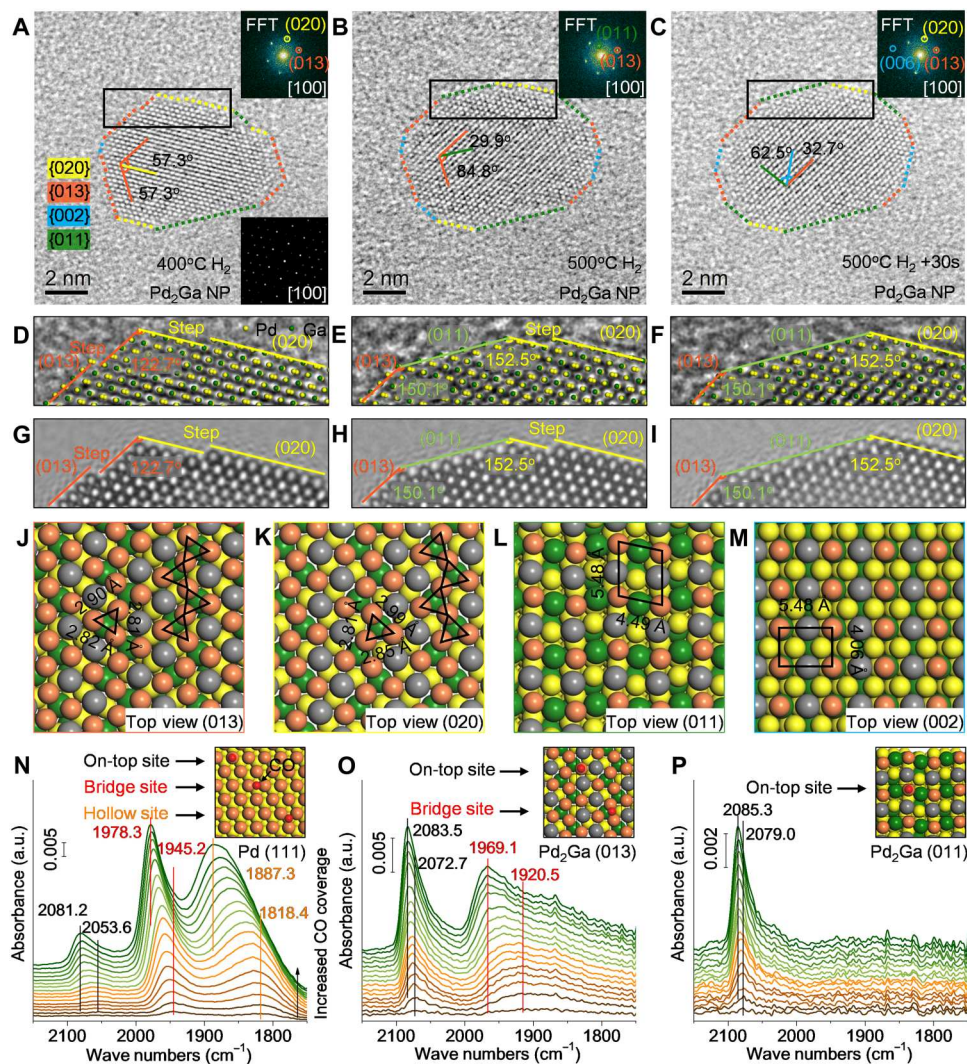


**Fig. 3. Surface atom arrangement and variation during Pd<sub>2</sub>Ga refacetting.** In situ HRTEM images of identical Pd<sub>2</sub>Ga NP at 400°C (A) and 500°C (B and C), respectively. The top-right and bottom insets are the corresponding FFTs and simulated SAED. (D to F) Enlarged TEM images overlapped with atomic models taken from the line boxes in (A) to (C). Simulated TEM images (G) to (I) correspond to (D) to (F). (J to M) Top view of the atomic models of (013), (020), (011), and (002) facets, respectively. (N to P) In situ CO-DRIFTS spectra with increased CO dose of Pd/Ga<sub>2</sub>O<sub>3</sub> samples after reduction at 100°, 300°, and 500°C. The top-right insets are the atomic models of CO adsorbed on surfaces with various Pd arrangements. Orange and gray, Pd and Ga atoms of the first layer; yellow and green, Pd and Ga atoms below the first layer.

displayed similar surface atom arrangement of Pd after different temperature reduction (figs. S25 and S26). In addition, because Pd<sub>2</sub>Ga is very prone to the oxidation (33, 38), it is crucial for clarifying its evolution in the ambient condition and its recoverability. The CO-DRIFTS (fig. S27) indicate that when 20% oxygen is introduced at room temperature, the on-top adsorption of CO disappears and only a small hollow adsorption remains. It suggests the destruction and oxidation of the isolated Pd<sub>1</sub> structure on the Pd<sub>2</sub>Ga surface. After further reduction at 100°C, all the on-top, bridge, and hollow adsorption peaks of CO appeared again, similar to the case of Pd structure. The intensity was greatly reduced, and the ratio of on-top sites increased, indicating that the Pd<sub>2</sub>Ga surface transforms to Pd and GaO<sub>x</sub> clusters (32, 38, 39). A further reduction at 500°C leads to the full recovering of the on-top adsorption peak of CO, indicating that the Pd<sub>2</sub>Ga surface was reconverted to the isolated Pd<sub>1</sub> pattern.

Complementarily, the in situ TEM and CO-DRIFTS results evidenced that the surface atom arrangement of Pd in Pd<sub>2</sub>Ga transforms from continuous Pd<sub>3</sub> to isolated Pd<sub>1</sub> at elevated temperatures.

### Underlying mechanism of Pd<sub>2</sub>Ga refacetting

The aforementioned results demonstrate the occurrence of refacetting and surface atom rearrangement of Pd<sub>2</sub>Ga at elevated temperatures under H<sub>2</sub> atmosphere. Following, theoretical calculations and models based on Pd<sub>2</sub>Ga were performed to investigate the underlying mechanism for this phenomenon. First, surface energies of generally observed Pd<sub>2</sub>Ga planes were calculated according to the previously reported method (40). As shown in Fig. 4A, the close-packed planes (210), (013), (211), (020), and (112) exhibit the lowest surface energies from 1.17 to 1.32 J m<sup>-2</sup>, while non-close-packed planes (223), (230), (002), and (011) exhibit the highest surface energies from 1.50 to 1.56 J m<sup>-2</sup>. Subsequently, the Wulff

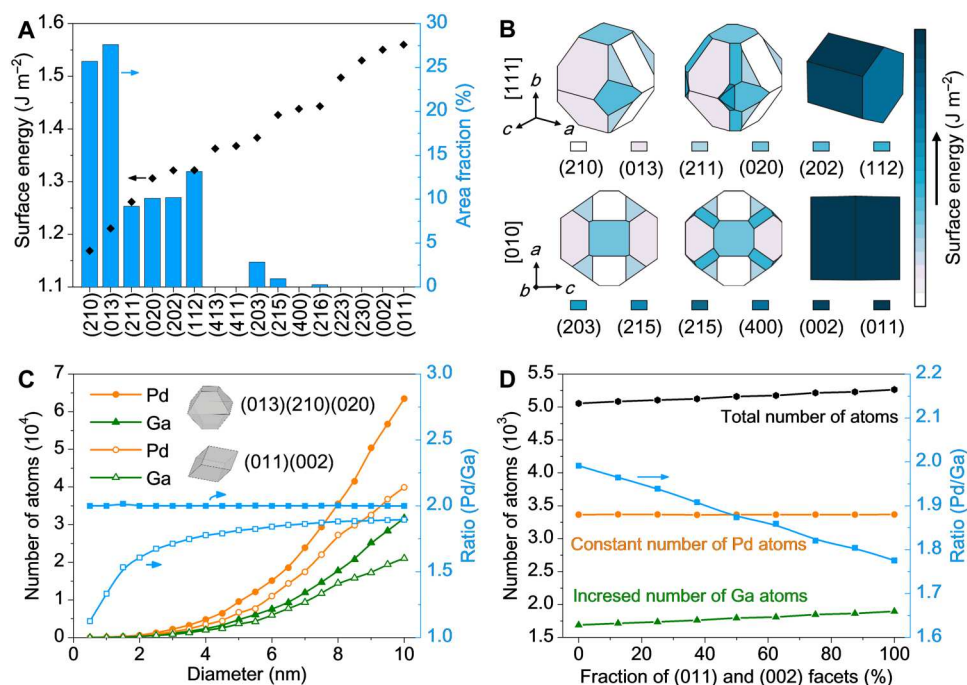


**Fig. 4. Morphological and stoichiometric variation of Pd<sub>2</sub>Ga NPs during refacetting.** (A) Calculated surface energies of Pd<sub>2</sub>Ga and their corresponding area fraction in Wulff shape. (B) Wulff shape of the Pd<sub>2</sub>Ga nanocrystal enclosed with different facets viewed from [111] and [010] directions. (C) Pd/Ga ratios in Pd<sub>2</sub>Ga atomic models enclosed with (013), (210), (020) and (011), and (002) as function of increased particle size. (D) The Ga atoms variation with the increased fraction of (011) and (002) facets in Pd<sub>2</sub>Ga atomic models with constant Pd atoms.

shape (Fig. 4B) was constructed using VESTA according to the obtained surface energies. The corresponding area fractions of Pd<sub>2</sub>Ga particle was acquired, in which nearly 97% area was enclosed by (210), (013), (211), (020), and (112) facets. An extreme case of Pd<sub>2</sub>Ga NPs consisting of (210), (013), (020), (202), (400), (002), and (011) facets were fully constructed. The Pd<sub>2</sub>Ga model NP enclosed with low surface energies exhibits similar morphology compared with Wulff shape. However, the model consistent with high surface energies is totally different. The amounts of Pd and Ga atoms in Pd<sub>2</sub>Ga NPs (0.5 to 10.0 nm) with the exposed (210), (013), (020), and (011) facets were fully studied from the created atomic models. As shown in Fig. 4C, the ratio between Pd and Ga remains 2.0 for the increase of particle size in Pd-rich facets enclosed NPs, in agreement with the stoichiometric Pd<sub>2</sub>Ga phase. However, the Pd/Ga ratio is always lower (<1.9) than the stoichiometric Pd<sub>2</sub>Ga when the NPs are enclosed with (011)/(002) planes. In addition, the value decreased markedly (1.1 to 1.7) as of the particle size <3 nm, attributed to the increased ratio of surface atoms in small NPs. In addition, the constant number of Pd atoms (3365, ~5 nm) in model NPs with decreased area fraction of Pd-rich facets were controlled to elucidate the variation of Ga atoms. As shown in Fig. 4D, the amount of Ga atoms increases from 1690 to 1897 as the fraction of (011) and (002) facets increases in the NP model. The ratios of Pd to Ga correspondingly decrease from 1.99 to 1.78 as the Ga atoms increased. Therefore, it is reasonably concluded that the initially formed Pd<sub>2</sub>Ga NPs, composed of (210), (013), (020), and (202) facets, exhibit the stoichiometric Pd to Ga ratio. However, more Ga atoms are reduced from the Ga<sub>2</sub>O<sub>3</sub> and incorporate into the Pd<sub>2</sub>Ga NPs as the reduction temperature rises. Therefore, it leads to the refacetting of Pd<sub>2</sub>Ga and the surface atom

arrangement that is patterned from the continuous Pd<sub>3</sub> to isolated Pd<sub>1</sub> atoms.

### Catalytic performance in acetylene hydrogenation reaction

Acetylene selective hydrogenation reaction is aiming at removing the trace amount of acetylene in ethylene industrially (41). Thus, high acetylene conversion in both the absence and presence of ethylene was adopted to well interpret the difference between three kinds of surface Pd atom arrangement. In this reaction, two main side products, over hydrogenation product ethane (C<sub>2</sub>H<sub>6</sub>) and polymerization products (in this term, only C<sub>4</sub> was detectable), impede the ethylene selectivity improvement. The continuous Pd, Pd<sub>3</sub>, and isolated Pd<sub>1</sub> sites of Pd/Ga<sub>2</sub>O<sub>3</sub> catalysts were controlled through reduction at 100°, 300°, and 500°C according to the above-mentioned results. As shown in Fig. 5A, in the absence of ethylene, a continuous surface Pd atom arrangement exhibits low selectivity toward overhydrogenation product ethane (11.5%) at 98.2% conversion, which is not so high compared to the continuously Pd<sub>3</sub> (2.9%) and isolated Pd<sub>1</sub> (<1%) sites of Pd<sub>2</sub>Ga. Whereas in the presence of excess ethylene (20%), the ethane selectivity increased from 2.9 to 27.4% and 11.5 to 63.8% for the continuous Pd<sub>3</sub> and Pd sites, respectively. The isolated Pd<sub>1</sub> sites of Pd<sub>2</sub>Ga remain with low ethane selectivity (6.5%) at 94.3% acetylene conversion. The selectivity difference in both the absence and presence of ethylene is ascribed to the competitive adsorption and reaction of ethylene, which was confined as π configuration on isolated Pd<sub>1</sub> sites and di-σ configuration on the continuous Pd and Pd<sub>3</sub> sites. The low C<sub>2</sub>H<sub>4</sub> selectivity in continuous Pd and Pd<sub>3</sub> are dominating because of excessive uptake of hydrogen by C<sub>2</sub> intermediates. In addition, Arrhenius plot for acetylene hydrogenation reaction over

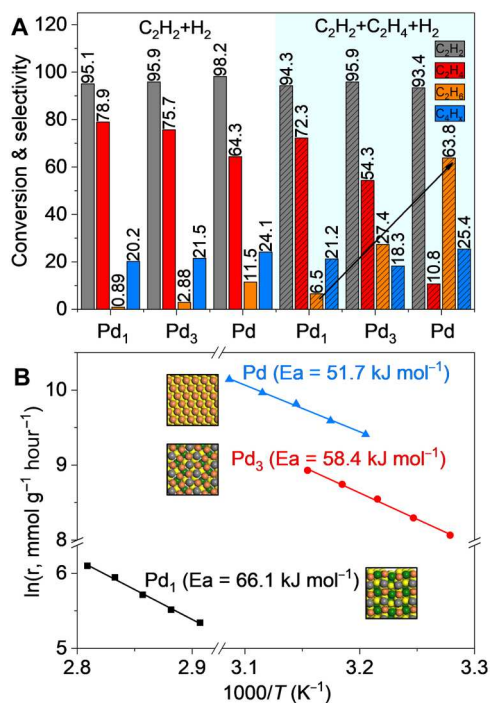


**Fig. 5. Hydrogenation properties of different surface Pd geometries.** (A) Conversion and selectivity in acetylene hydrogenation reaction of Pd-Ga<sub>2</sub>O<sub>3</sub>-based catalysts in the absence and presence of ethylene. (B) Arrhenius plot for acetylene hydrogenation reaction over various Pd geometries.

various Pd sites was performed to estimate the activation energies (Fig. 5B). The Pd/Ga<sub>2</sub>O<sub>3</sub> catalyst with continuous Pd sites on the surface exhibits the lowest apparent activation energy ( $E_a$ ) of 51.7 kJ mol<sup>-1</sup>, well comparable with the previous studies (41). The value of  $E_a$  increased to 58.4 and 66.1 kJ mol<sup>-1</sup> with further isolation of Pd atoms on the surface to Pd<sub>3</sub> and Pd<sub>1</sub> sites of supported Pd<sub>2</sub>Ga NP. It implies a decreased activity and is largely ascribed to the decreased ability to dissociate and activate hydrogen. Although Pd in Pd<sub>2</sub>Ga does not change much, its capability is still greatly reduced to activate hydrogen. This is due to the decrease in the amount of atoms in Pd ensembles on the surface (7, 42). The intrinsic activity markedly decreased as Pd atoms are isolated on the surface, displaying 1334.45, 346.96, and 7.39 min<sup>-1</sup> at 80°C for Pd, Pd<sub>3</sub>, and Pd<sub>1</sub> sites, respectively. However, the selectivity of ethylene and hydrogenation efficiency were extremely increased, especially in the presence of excess ethylene (Fig. 5A, vide infra). The hydrogenation efficiencies of different surface Pd atom arrangements were evaluated under high conversion of acetylene (by controlling the gas hourly space velocity) in both the absence and presence of ethylene (fig. S28). For Pd<sub>1</sub> sites of Pd<sub>2</sub>Ga/Ga<sub>2</sub>O<sub>3</sub> catalysts, the mass-specific activity was nearly constant in the introduction of excess ethylene (100 to 99%), which means that all the surface Pd<sub>1</sub> sites were used for the acetylene hydrogenation reaction. While for the continuous Pd<sub>3</sub> and Pd sites, the efficiencies of mass-specific activity in acetylene hydrogenation decreased from 100 to ~82% and ~64%, respectively. The decreased activities on the surface of Pd and Pd<sub>2</sub>Ga with the continuous Pd<sub>3</sub> sites implies that some active sites are not used for the adsorption and reaction of acetylene. It is ascribed to the increased coverage of intermediate

product ethynylidyne as the excess of ethylene is introduced (43, 44). As a result, the amount of converted acetylene is significantly reduced, hindering the effective utilization of active sites. In addition, the increased selectivity of ethane (~20 to 30% of Pd<sub>3</sub> and ~40 to 60% of Pd) further decreases the efficiency of the desired hydrogenation pathway to ethylene. The activity and selectivity of Pd<sub>2</sub>Ga catalysts with continuous Pd<sub>3</sub> and isolated Pd<sub>1</sub> sites remain after a 24-hour test (figs. S29 and S30), revealing that Pd<sub>2</sub>Ga structure is relatively stable during the acetylene hydrogenation reaction and well consistent with previous studies (45, 46). For the thermogravimetric results of Pd<sub>2</sub>Ga catalysts with isolated Pd<sub>1</sub> site, no weight loss or coke deposition was determined by thermogravimetric experiment in either direct reduced or used Pd<sub>2</sub>Ga catalyst with isolated Pd<sub>1</sub> site (fig. S31). Weight increases of ~0.7% for both the samples after 700°C treatment could be ascribed to the oxidation of Pd<sub>2</sub>Ga. Last, the stability of supported Pd<sub>2</sub>Ga NPs was verified by ETEM and in situ DRIFTS experiments. As shown in fig. S32, the Pd<sub>2</sub>Ga NPs exhibit the Wulff shape after 350°C reduction, which was encapsulated of (210), (013), (012), and (202) facets with the continuous Pd sites, and the morphology was maintained during and after reaction. The identical Pd<sub>2</sub>Ga NP also kept its shape after reduction at 500°C and reaction, which mainly enclosed with (323), (313), and (016) facets and exposed with isolated Pd<sub>1</sub> sites (fig. S33). Following, the in situ CO-DRIFTS experiments (fig. S34) were conducted to monitor the surface structural variation before and after reaction. The results exhibit that the consecutive Pd<sub>3</sub> and Pd<sub>1</sub> surface atom arrangements remained stable during acetylene hydrogenation reaction. The bridge and on-top adsorption of CO remained constant before and after the reaction on two kinds of Pd<sub>2</sub>Ga catalysts, which were respectively obtained by reduction at 300° and 500°C. Thus, both in situ structural characterizations and long-time reaction tests indicate that the formed surface structures of supported Pd<sub>2</sub>Ga NPs are stable during the acetylene hydrogenation reaction.

## DISCUSSION

In conclusion, we demonstrate that the surface atom arrangement of Pd<sub>2</sub>Ga can be controlled via the temperature-promoted RMSI. Both XRD and TEM investigations prove the structural evolution from Pd to Pd<sub>2</sub>Ga after the reduction and inclusion of Ga atoms. In situ atomic-scale ADF-STEM, STEM simulation, and EDX elemental mapping explicitly confirm the formation of highly ordered orthorhombic Pd<sub>2</sub>Ga phase. ETEM directly visualizes surface restructuring of the identical NP from (013) and (020) to (011) and (002) at elevated temperatures. It was found that the surface atom arrangements of Pd transforms from the continuous Pd<sub>3</sub> to isolated Pd<sub>1</sub> geometries. Sample-averaged information from CO-DRIFTS evidences the existence of both on-top and bridge adsorption of CO on Pd<sub>2</sub>Ga after 300°C reduction, whereas only on-top adsorption of CO remained after 500°C reduction. Complementarily, it proves the surface atom arranging variation from Pd<sub>3</sub> to Pd<sub>1</sub> atoms of Pd<sub>2</sub>Ga. Moreover, the surface energy calculation and modeling simulation show that the initially formed Pd<sub>2</sub>Ga NPs are encapsulated with a low-energy Pd-rich surface. The atomic ratio of the Pd<sub>2</sub>Ga NPs is basically stoichiometric. When the temperature increases, more Ga atoms are reduced and arranged on the surface. As a result, it leads to surface restructuring and the increase of Ga content in the NPs, which is slightly beyond the

stoichiometric ratio of Pd<sub>2</sub>Ga. A similar phenomenon, to the best of our knowledge, would occur in other RMSI systems throughout a temperature range. Stronger reduction conditions would cause more support to be reduced after the initial formation of the intermetallic NPs. However, because it is inadequate for the temperature and amount of the additional reduced atoms to form a new phase, these atoms tend to arrange on the surface to maintain the intermetallic structure. Thus, it will lead to the surface restructuring of the intermetallic NP. In acetylene hydrogenation reaction, Pd<sub>2</sub>Ga with surface Pd<sub>3</sub> sites shows improved mass-specific activity compared to Pd<sub>1</sub> sites, which may result from the strong capability to activate and dissociate molecule hydrogen of Pd ensemble sites. Pd<sub>2</sub>Ga with surface Pd<sub>1</sub> sites displays the improved selectivity and atomic efficiency, ascribed to a weakened adsorption of ethylene with confined  $\pi$  configuration. Hence, our work provides ultimate understanding of temperature-promoted RMSI and a proof of concept to facile and delicate control of the surface atom arrangement of supported intermetallic NPs. Such merits are promising to be applied in design of other heterogeneous catalysts.

## MATERIALS AND METHODS

### Materials preparation

The GaOOH nanorods were synthesized using a typical solvothermal method, 1050 mg of sodium dodecylbenzenesulfonate and 3850 mg of gallium nitrate hydrate were dissolved in 60 ml of deionized water under vigorous stirring. The mixture was stirred in air for 3 min to form a white slurry. Then, the 1.5 M sodium hydroxide (Sinopharm Chemical Reagent, CO) was dropwise added to the solution until the pH was 7 to 8. Then, the mixture was stirred for about 5 min to obtain a white flocculated colloid. Then, the suspension was transferred into a 100-ml autoclave, sealed, and maintained at 140°C for 8 hours. The acquired mixtures were filtered and washed three times with deionized water after being lowered to room temperature. The obtained white powder was dried in the oven at 80°C for 12 hours and then calcined at 300, 500, 700, and 900°C for 2 hours.

The supported catalyst was prepared through a typical wetness impregnation method, during which the palladium acetylacetonate (Sigma-Aldrich) and  $\alpha$ -Ga<sub>2</sub>O<sub>3</sub> nanorods were used. The loading content of Pd was controlled at 5.0 weight %. After calcination at 500°C in air for 2 hours, the samples were reduced at 100° to 600°C with a 100°C interval in 50% H<sub>2</sub>/Ar for 2 hours to obtain the metallic Pd-based catalysts.

### TEM investigations

For ex situ TEM characterization, a typical sample preparation process was performed by depositing dispersed samples onto holey copper/carbon grids. A FEI Tecnai G<sup>2</sup> F20 microscope working at 200 kV was used for preliminarily microstructural studies.

In situ TEM investigations were conducted on the Titan Themis G3 ETEM with a Cs corrector working at 300 kV. The TEM images were recorded by a Gatan OneView camera with a dose rate less than  $\sim 300 \text{ e}^{-}\text{\AA}^2 \text{ s}^{-1}$  during the experiments. During the in situ TEM experiments, the pressure of H<sub>2</sub> in the vicinity of the sample was controlled at about 300 Pa through the differential apertures and pumps. The PdO/Ga<sub>2</sub>O<sub>3</sub> sample was used and loaded onto a heating holder (FEI Nano-Ex) and in situ reduced at 200°C to

acquire the metallic Pd. It was elevated to 300°C at a rate of 10°C/min to monitor the transformation process. Following, the temperature was sequentially elevated and kept at 300°, 400°, and 500°C for in situ structural characterizations. In situ TEM experiments were also conducted to determine the structural change of Pd<sub>2</sub>Ga samples, which were respectively reduced at 350° and 500°C under 200 Pa H<sub>2</sub>, during and after catalysis. The reaction atmosphere in ETEM was controlled as 7 Pa of acetylene and 70 Pa of hydrogen, and the reaction temperature is 200°C.

In situ STEM studies were also performed on a Cs-corrected Hitachi HF5000 microscope equipped with EDX, secondary electron, and ADF detectors at 200 kV. The gas atmosphere was flowed into the column of TEM near the sample through a nozzle, and the pressure was controlled to less than  $\sim 10$  Pa during the experiment. The heating experiments were achieved by a micro-electromechanical system-based holder developed by Hitachi. Temperatures of 300° and 500°C were respectively kept for both STEM and EDX imaging. The atomic models of Pd<sub>2</sub>Ga NPs were established by ATOMS software, and the HRTEM and SAED simulations were carried out on JEMS software (copyright P. Stadelmann 2014-2020, JEMS-SWISS). The STEM simulations were performed using Dr. Probe software (47).

### CO-DRIFTS investigations

The CO-DRIFTS experiments were conducted on Thermo Fisher Scientific NICOLET iZ10 with an in situ DRIFT reaction cell (Harrick Scientific Products), and the spectrum was recorded at a resolution of  $4 \text{ cm}^{-1}$ . The PdO/Ga<sub>2</sub>O<sub>3</sub> samples were diluted with KBr (PdO/Ga<sub>2</sub>O<sub>3</sub>:KBr = 1:9 or 1:0) and ground before loading into the cell, then in situ reduced at 100°, 300°, and 500°C in 50 volume percent (volume %) H<sub>2</sub>/He (20 ml/min) or 50 volume % H<sub>2</sub>/Ar for 2 hours. After cooling down 20°C, helium (20 ml/min) was introduced to remove the residue H<sub>2</sub> and obtain the background spectrum. Then, CO/He was gradually (1 ml of 5.0 volume % CO/He for 10 s) introduced to the in situ cell to obtain the CO adsorbed spectrum for Pd-based catalysts. The CO partial pressure were also controlled from 1.2 to 50 mbar during the experiments. After obtaining the supported Pd<sub>2</sub>Ga NPs with varied surface structures at 300° and 500°C, the reaction gases (10 ml/min, 0.1 mbar C<sub>2</sub>H<sub>2</sub>, 1 mbar H<sub>2</sub>, and He as balance) were introduced to the reaction cell for 60 min. The CO and C<sub>2</sub>H<sub>2</sub> adsorbed spectra were collected before (20°C), during (150°C), and after (20°C) the reaction.

### Catalytic tests

The acetylene selective hydrogenation in the absence and presence of excess ethylene (1.0 volume % C<sub>2</sub>H<sub>2</sub>, 10 volume % H<sub>2</sub>, helium as balance and 0.5 volume % C<sub>2</sub>H<sub>2</sub>, 5.0 to 10.0 volume % H<sub>2</sub>, 20.0 volume % C<sub>2</sub>H<sub>4</sub>, helium as balance) was performed in a fixed-bed quartz microreactor under atmospheric pressure. The PdO/Ga<sub>2</sub>O<sub>3</sub> (0.1, 0.3, and 3.0 mg) was in situ reduced at 100°, 300°, and 500°C with a ramp rate of 10°C/min under 50 volume % H<sub>2</sub>/He atmosphere before the reaction tests. The reaction temperatures were controlled at 80°, 80°, and 135°C for Pd, Pd<sub>3</sub>, and Pd<sub>1</sub> catalysts, respectively. The flow rate was set from 10 to 70 ml/min, and the acetylene conversion was controlled below 10% during the kinetic experiments. The stability tests were conducted at both 140° and 200°C for Pd<sub>2</sub>Ga exposed with the continuous Pd<sub>3</sub> and isolated Pd<sub>1</sub> sites. The amount of acetylene, ethylene, ethane, 1-butene, isobutene, *cis*-2-butene, *trans*-2-butene, and butadiene was detected by

an Agilent Technologies 7890A gas chromatograph equipped with a flame ionization detector. The conversion and selectivity of the reaction were calculated according to Eqs. 1 to 4

$$\text{Conv}_{\text{C}_2\text{H}_2} = \frac{C_{\text{C}_2\text{H}_2,\text{in}} - C_{\text{C}_2\text{H}_2,\text{out}}}{C_{\text{C}_2\text{H}_2,\text{in}}} \times 100\% \quad (1)$$

$$\text{Sele}_{\text{C}_2\text{H}_4} = \left(1 - \frac{C_{\text{C}_2\text{H}_6,\text{out}} + 2C_{\text{C}_4\text{H}_x,\text{out}}}{C_{\text{C}_2\text{H}_2,\text{in}} - C_{\text{C}_2\text{H}_2,\text{out}}}\right) \times 100\% \quad (2)$$

$$\text{Sele}_{\text{C}_2\text{H}_6} = \frac{C_{\text{C}_2\text{H}_6,\text{out}} - C_{\text{C}_2\text{H}_6,\text{in}}}{C_{\text{C}_2\text{H}_2,\text{in}} - C_{\text{C}_2\text{H}_2,\text{out}}} \times 100\% \quad (3)$$

$$\text{Sele}_{\text{C}_4\text{H}_x} = \frac{C_{\text{C}_4\text{H}_x,\text{out}}}{C_{\text{C}_2\text{H}_2,\text{in}} - C_{\text{C}_2\text{H}_2,\text{out}}} \times 100\% \quad (4)$$

where  $C_{\text{in}}$  represents the acetylene concentration in the feed gas and  $C_{\text{out}}$  denotes the different products in the outlet gas. The  $\text{C}_4\text{H}_x$  represents the overall polymerization product that contained the 1-butene, isobutene, *cis*-2-butene, *trans*-2-butene, and butadiene.

The atomic models of Pd and Pd<sub>2</sub>Ga NP (5 to 6 nm), which contain ~9100 to 12,000 Pd atoms, were established to determine the amounts of surface Pd atoms. The dispersions ( $D$ ) of Pd and Pd<sub>2</sub>Ga NPs exposed with the continuous Pd<sub>3</sub> and isolated Pd<sub>1</sub> sites were calculated as 0.1933, 0.2274, and 0.1074, respectively. The turnover frequencies (TOFs) were calculated by the following equation

$$\text{TOFs} = \frac{\text{Mole of C}_2\text{H}_2 \text{ converted per minute}}{D \times n_{\text{Pd}}} \times 100\%$$

where  $D$  is the dispersion of Pd-based NPs and  $n_{\text{Pd}}$  is the mole of Pd.

### Computational details

The spin-polarized density functional theories were performed using the Vienna Ab Initio Simulation Package (48). The Perdew-Burke-Ernzerhof generalized gradient approximation functional was used to describe the exchange-correlation energy (49). The energy cutoff was set to 400 eV. The Monkhorst-Pack  $k$ -points grid was set to be  $k_1 \times k_2 \times 1$  ( $a \cdot k_1 \geq 30$ ,  $b \cdot k_2 \geq 30$ ) for the slab model calculations. The vacuum region was set to be 15 Å in the  $z$  direction to minimize the interactions between the periodic slabs. The energy convergence and atomic forces were set to  $10^{-6}$  eV and 0.02 eV/Å, respectively. The surface energy  $\gamma_s$  is the energy required to cleave a surface from the bulk phase, which describes the stability of the surface. The  $\gamma_s$  is calculated by the equation below (50)

$$\gamma_s = \frac{1}{2A}(E_s^{\text{unrel}} - N E_b/N_b) - \frac{1}{A}(E_s^{\text{rel}} - E_s^{\text{unrel}})$$

where  $A$  is the area of the surface.  $E_s^{\text{unrel}}$  and  $E_s^{\text{rel}}$  are the energies of the unrelaxed and relaxed surfaces, respectively.  $N$  and  $N_b$  are the atom number for the slab model and original cell, respectively.  $E_b$  is the energy for the original cell.

### Thermogravimetric analysis

The thermogravimetric analysis experiments were performed using a Netzsch STA 449 F3 instrument. The reduced and spent Pd<sub>2</sub>Ga/

Ga<sub>2</sub>O<sub>3</sub> catalysts (~5 mg) were treated under 50% O<sub>2</sub>/Ar flow (40 ml/min) from 40° to 700°C with a ramp rate of 5°C/min.

### XRD investigations

The XRD measurements were performed on a Rigaku D/Max 2400 diffractometer (Cu K $\alpha$  radiation,  $\lambda = 0.15418$  nm) operated at 40 kV and 40 mA.

### Supplementary Materials

This PDF file includes:

Figs. S1 to S34

[View/request a protocol for this paper from Bio-protocol.](#)

### REFERENCES AND NOTES

- S. Tian, Q. Fu, W. Chen, Q. Feng, Z. Chen, J. Zhang, W. C. Cheong, R. Yu, L. Gu, J. Dong, J. Luo, C. Chen, Q. Peng, C. Draxl, D. Wang, Y. Li, Carbon nitride supported Fe<sub>2</sub> cluster catalysts with superior performance for alkene epoxidation. *Nat. Commun.* **9**, 2353 (2018).
- X. Zhang, M. Zhang, Y. Deng, M. Xu, L. Artiglia, W. Wen, R. Gao, B. Chen, S. Yao, X. Zhang, M. Peng, J. Yan, A. Li, Z. Jiang, X. Gao, S. Cao, C. Yang, A. J. Kropf, J. Shi, J. Xie, M. Bi, J. A. van Bokhoven, Y. W. Li, X. Wen, M. Flytzani-Stephanopoulos, C. Shi, W. Zhou, D. Ma, A stable low-temperature H<sub>2</sub>-production catalyst by crowding Pt on  $\alpha$ -MoC. *Nature* **589**, 396–401 (2021).
- S. Dai, J. P. Chou, K. W. Wang, Y. Y. Hsu, A. Hu, X. Pan, T. Y. Chen, Platinum-trimer decorated cobalt-palladium core-shell nanocatalyst with promising performance for oxygen reduction reaction. *Nat. Commun.* **10**, 440 (2019).
- B. Qiao, A. Wang, X. Yang, L. F. Allard, Z. Jiang, Y. Cui, J. Liu, J. Li, T. Zhang, Single-atom catalysis of CO oxidation using Pt<sub>1</sub>/FeO<sub>x</sub>. *Nat. Chem.* **3**, 634–641 (2011).
- J. Jones, H. Xiong, A. T. DeLaRiva, E. J. Peterson, H. Pham, S. R. Challa, G. Qi, S. Oh, M. H. Wiebenga, X. I. Pereira Hernandez, Y. Wang, A. K. Datye, Thermally stable single-atom platinum-on-ceria catalysts via atom trapping. *Science* **353**, 150–154 (2016).
- L. Lin, W. Zhou, R. Gao, S. Yao, X. Zhang, W. Xu, S. Zheng, Z. Jiang, Q. Yu, Y. W. Li, C. Shi, X. D. Wen, D. Ma, Low-temperature hydrogen production from water and methanol using Pt/ $\alpha$ -MoC catalysts. *Nature* **544**, 80–83 (2017).
- G. Kyriakou, M. B. Boucher, A. D. Jewell, E. A. Lewis, T. J. Lawton, A. E. Baber, H. L. Tierney, M. Flytzani-Stephanopoulos, E. C. H. Sykes, Isolated metal atom geometries as a strategy for selective heterogeneous hydrogenations. *Science* **335**, 1209–1212 (2012).
- M. Ouyang, K. G. Papanikolaou, A. Boubnov, A. S. Hoffman, G. Giannakakis, S. R. Bare, M. Stamatakis, M. Flytzani-Stephanopoulos, E. C. H. Sykes, Directing reaction pathways via in situ control of active site geometries in PdAu single-atom alloy catalysts. *Nat. Commun.* **12**, 1549 (2021).
- H. Wang, Q. Luo, W. Liu, Y. Lin, Q. Guan, X. Zheng, H. Pan, J. Zhu, Z. Sun, S. Wei, J. Yang, J. Lu, Quasi Pd<sub>1</sub>Ni single-atom surface alloy catalyst enables hydrogenation of nitriles to secondary amines. *Nat. Commun.* **10**, 4998 (2019).
- W. Ren, X. Tan, W. Yang, C. Jia, S. Xu, K. Wang, S. C. Smith, C. Zhao, Isolated diatomic Ni-Fe metal-nitrogen sites for synergistic electroreduction of CO<sub>2</sub>. *Angew. Chem. Int. Ed.* **58**, 6972–6976 (2019).
- J. Fu, J. Dong, R. Si, K. Sun, J. Zhang, M. Li, N. Yu, B. Zhang, M. G. Humphrey, Q. Fu, J. Huang, Synergistic effects for enhanced catalysis in a dual single-atom catalyst. *ACS Catal.* **11**, 1952–1961 (2021).
- Y. Ma, Y. Ren, Y. Zhou, W. Liu, W. Baaziz, O. Ersen, C. Pham-Huu, M. Greiner, W. Chu, A. Wang, T. Zhang, Y. Liu, High-density and thermally stable palladium single-atom catalysts for chemoselective hydrogenations. *Angew. Chem. Int. Ed.* **59**, 21613–21619 (2020).
- H. Jeong, O. Kwon, B.-S. Kim, J. Bae, S. Shin, H.-E. Kim, J. Kim, H. Lee, Highly durable metal ensemble catalysts with full dispersion for automotive applications beyond single-atom catalysts. *Nat. Catal.* **3**, 368–375 (2020).
- J. Prinz, R. Gaspari, Q. S. Stockl, P. Gille, M. Armbruster, H. Brune, O. Groning, C. A. Pignedoli, D. Passerone, R. Widmer, Ensemble effect evidenced by CO adsorption on the 3-fold PdGa surfaces. *J. Phys. Chem. C* **118**, 12260–12265 (2014).
- A.-X. Yin, X.-Q. Min, Y.-W. Zhang, C.-H. Yan, Shape-selective synthesis and facet-dependent enhanced electrocatalytic activity and durability of monodisperse sub-10 nm Pt–Pd tetrahedrons and cubes. *J. Am. Chem. Soc.* **133**, 3816–3819 (2011).
- J. Zhang, H. Yang, J. Fang, S. Zou, Synthesis and oxygen reduction activity of shape-controlled Pt<sub>3</sub>Ni nanopolyhedra. *Nano Lett.* **10**, 638–644 (2010).
- D. S. Su, B. Zhang, R. Schlogl, Electron microscopy of solid catalysts—Transforming from a challenge to a toolbox. *Chem. Rev.* **115**, 2818–2882 (2015).

18. F. F. Tao, P. A. Crozier, Atomic-scale observations of catalyst structures under reaction conditions and during catalysis. *Chem. Rev.* **116**, 3487–3539 (2016).
19. Y. M. Niu, B. S. Zhang, In situ investigation of nanocatalysts in gas atmosphere by transmission electron microscopy. *Curr. Opin. Green Sust. Chem.* **22**, 22–28 (2020).
20. S. Zhang, P. N. Plessow, J. J. Willis, S. Dai, M. Xu, G. W. Graham, M. Cargnello, F. Abild-Pedersen, X. Pan, Dynamical observation and detailed description of catalysts under strong metal-support interaction. *Nano Lett.* **16**, 4528–4534 (2016).
21. A. Beck, X. Huang, L. Artiglia, M. Zabilskiy, X. Wang, P. Rzepka, D. Palagin, M. G. Willinger, J. A. van Bokhoven, The dynamics of overlayer formation on catalyst nanoparticles and strong metal-support interaction. *Nat. Commun.* **11**, 3220 (2020).
22. S. B. Vendelbo, C. F. Elkjaer, H. Falsig, I. Puspitasari, P. Dona, L. Mele, B. Morana, B. J. Nelissen, R. van Rijn, J. F. Creemer, P. J. Kooyman, S. Helveg, Visualization of oscillatory behaviour of Pt nanoparticles catalysing CO oxidation. *Nat. Mater.* **13**, 884–890 (2014).
23. H. Yoshida, Y. Kuwauchi, J. R. Jinschek, K. Sun, S. Tanaka, M. Kohyama, S. Shimada, M. Haruta, S. Takeda, Visualizing gas molecules interacting with supported nanoparticle catalysts at reaction conditions. *Science* **335**, 317–319 (2012).
24. W. Yuan, B. Zhu, X.-Y. Li, T. W. Hansen, Y. Ou, K. Fang, H. Yang, Z. Zhang, J. B. Wagner, Y. Gao, Y. Wang, Visualizing H<sub>2</sub>O molecules reacting at TiO<sub>2</sub> active sites with transmission electron microscopy. *Science* **367**, 428–430 (2020).
25. X. Zhang, J. Meng, B. Zhu, J. Yu, S. Zou, Z. Zhang, Y. Gao, Y. Wang, In situ TEM studies of the shape evolution of Pd nanocrystals under oxygen and hydrogen environments at atmospheric pressure. *Chem. Commun.* **53**, 13213–13216 (2017).
26. X. Zhang, J. Meng, B. Zhu, W. Yuan, H. Yang, Z. Zhang, Y. Gao, Y. Wang, Unexpected refaceting of palladium nanoparticles under atmospheric N<sub>2</sub> conditions. *Chem. Commun.* **54**, 8587–8590 (2018).
27. S. W. Chee, J. M. Arce-Ramos, W. Li, A. Genest, U. Mirsaidov, Structural changes in noble metal nanoparticles during CO oxidation and their impact on catalyst activity. *Nat. Commun.* **11**, 2133 (2020).
28. Y. Niu, X. Liu, Y. Wang, S. Zhou, Z. Lv, L. Zhang, W. Shi, Y. Li, W. Zhang, D. S. Su, B. Zhang, Visualizing formation of intermetallic PdZn in a palladium/zinc oxide catalyst: Interfacial fertilization by PdH<sub>x</sub>. *Angew. Chem. Int. Ed.* **58**, 4232–4237 (2019).
29. L. Li, B. Zhang, E. Kunkes, K. Föttinger, M. Armbrüster, D. S. Su, W. Wei, R. Schlögl, M. Behrens, Ga-Pd/Ga<sub>2</sub>O<sub>3</sub> catalysts: The role of gallia polymorphs, intermetallic compounds, and pretreatment conditions on selectivity and stability in different reactions. *ChemCatChem* **4**, 1764–1775 (2012).
30. Y. Quan, D. Fang, X. Zhang, S. Liu, K. Huang, Synthesis and characterization of gallium oxide nanowires via a hydrothermal method. *Mater. Chem. Phys.* **121**, 142–146 (2010).
31. K. Kovnir, M. Schmidt, C. Waurisch, M. Armbrüster, Y. Prots, Y. Grin, Refinement of the crystal structure of dipalladium gallium, Pd<sub>2</sub>Ga. *Zeitschrift Fur Krist. New Cryst. Struct.* **223**, 7–8 (2008).
32. R. Leary, F. de la Peña, J. S. Barnard, Y. Luo, M. Armbrüster, J. Meurig Thomas, P. A. Midgley, Revealing the atomic structure of intermetallic GaPd<sub>2</sub> nanocatalysts by using aberration-corrected scanning transmission electron microscopy. *ChemCatChem* **5**, 2599–2609 (2013).
33. G. Wowsnick, D. Teschner, M. Armbrüster, I. Kasatkin, F. Girgsdies, Y. Grin, R. Schlögl, M. Behrens, Surface dynamics of the intermetallic catalyst Pd<sub>2</sub>Ga, Part II—Reactivity and stability in liquid-phase hydrogenation of phenylacetylene. *J. Catal.* **309**, 221–230 (2014).
34. Y. Wang, Y. Niu, T. Gao, S. Liu, B. Zhang, Assessing the effect of the electron-beam irradiation on Pd/Ga<sub>2</sub>O<sub>3</sub> catalyst under ambient pressure. *ChemCatChem* **12**, 4765–4769 (2020).
35. C. Lamberti, A. Zecchina, E. Groppo, S. Bordiga, Probing the surfaces of heterogeneous catalysts by in situ IR spectroscopy. *Chem. Soc. Rev.* **39**, 4951–5001 (2010).
36. C. D. Zeinalipour-Yazdi, D. J. Willock, L. Thomas, K. Wilson, A. F. Lee, CO adsorption over Pd nanoparticles: A general framework for IR simulations on nanoparticles. *Sur. Sci.* **646**, 210–220 (2016).
37. K. Föttinger, G. Rupprechter, In situ spectroscopy of complex surface reactions on supported Pd-Zn, Pd-Ga, and Pd(Pt)-Cu nanoparticles. *Accounts Chem. Res.* **47**, 3071–3079 (2014).
38. G. Wowsnick, D. Teschner, I. Kasatkin, F. Girgsdies, M. Armbrüster, A. Zhang, Y. Grin, R. Schlögl, M. Behrens, Surface dynamics of the intermetallic catalyst Pd<sub>2</sub>Ga, Part I—Structural stability in UHV and different gas atmospheres. *J. Catal.* **309**, 209–220 (2014).
39. A. Haghofer, K. Föttinger, M. Nachtegaal, M. Armbrüster, G. Rupprechter, Microstructural changes of supported intermetallic nanoparticles under reductive and oxidative conditions: An in situ x-ray absorption study of Pd/Ga<sub>2</sub>O<sub>3</sub>. *J. Phys. Chem. C* **116**, 21816–21827 (2012).
40. R. Tran, Z. Xu, B. Radhakrishnan, D. Winston, W. Sun, K. A. Persson, S. P. Ong, Surface energies of elemental crystals. *Sci. Data* **3**, 160080 (2016).
41. A. Borodziński, G. C. Bond, Selective hydrogenation of ethyne in ethene-rich streams on palladium catalysts. Part 1. Effect of changes to the catalyst during reaction. *Catal. Rev.* **48**, 91–144 (2006).
42. S. Liu, Y. Niu, Y. Wang, J. Chen, X. Quan, X. Zhang, B. Zhang, Unravelling the role of active-site isolation in reactivity and reaction pathway control for acetylene hydrogenation. *Chem. Commun.* **56**, 6372–6375 (2020).
43. D. Mei, Z. Neurock, C. M. Smith, Hydrogenation of acetylene–ethylene mixtures over Pd and Pd–Ag alloys: First-principles-based kinetic Monte Carlo simulations. *J. Catal.* **268**, 181–195 (2009).
44. D. Mei, P. A. Sheth, M. Neurock, C. M. Smith, First-principles-based kinetic Monte Carlo simulation of the selective hydrogenation of acetylene over Pd(111). *J. Catal.* **242**, 1–15 (2006).
45. L. Shao, W. Zhang, M. Armbrüster, D. Teschner, F. Girgsdies, B. Zhang, O. Timpe, M. Friedrich, R. Schlögl, D. S. Su, Nanosizing intermetallic compounds onto carbon nanotubes: Active and selective hydrogenation catalysts. *Angew. Chem. Int. Ed.* **50**, 10231–10235 (2011).
46. Y. Luo, S. Alarcón Villaseca, M. Friedrich, D. Teschner, A. Knop-Gericke, M. Armbrüster, Addressing electronic effects in the semi-hydrogenation of ethyne by InPd<sub>2</sub> and intermetallic Ga–Pd compounds. *J. Catal.* **338**, 265–272 (2016).
47. J. Barthel, Dr. Probe: A software for high-resolution STEM image simulation. *Ultramicroscopy* **193**, 1–11 (2018).
48. G. Kresse, J. Furthmüller, Efficiency of ab-initio total energy calculations for metals and semiconductors using a plane-wave basis set. *Comp. Mater. Sci.* **6**, 15–50 (1996).
49. J. P. Perdew, K. Burke, M. Ernzerhof, Generalized gradient approximation made simple. *Phys. Rev. Lett.* **77**, 3865–3868 (1996).
50. Q. Li, M. Rellán-Piñero, N. Almora-Barrios, M. García-Ratés, I. N. Remediakis, N. López, Shape control in concave metal nanoparticles by etching. *Nanoscale* **9**, 13089–13094 (2017).

**Acknowledgments:** We thank M. Hiroaki (Hitachi HF5000, Hitachi High-Technologies Co. Ltd) for help in the in situ STEM experiments. **Funding:** This work was supported by National Natural Science Foundation of China grant nos. 22072164, 22002173, 52161145403, 51932005, 21761132025, and 21972140; Postdoctoral Science Foundation of China grant no. 2020M680999; Liaoning Revitalization Talents Program grant nos. XLYC1807175 and XLYC1907053; and the Research Fund of SYNLU. **Author contributions:** Y.N. and B.Z. conceived and designed the experiments and carried out the structural and catalytic performance analysis. Y.N. and Y.W. prepared the Pd/Ga<sub>2</sub>O<sub>3</sub> catalysts and performed the reaction test experiments. J.C. and Y.N. conducted the theory calculation experiment and data analysis. Y.N., Y.W., S.L., Y.L., X.H., W.Z., M.-G.W., and B.Z. contributed to the in situ TEM experiments and structural analysis. Y.N. and Y.W. conducted the XRD experiments and structural analysis. Y.N. and Y.W. carried out the in situ CO-DRIFTS experiments and data analysis. B.Z., W.Z., and Y.N. conducted the HRTEM, SAED, and STEM simulation. All authors contributed to the discussions and manuscript preparation. **Competing interests:** The authors declare that they have no competing interests. **Data and materials availability:** All data needed to evaluate the conclusions in the paper are present in the paper and/or the Supplementary Materials.

Submitted 18 April 2022  
Accepted 3 November 2022  
Published 9 December 2022  
10.1126/sciadv.abq5751